Materials Science & Engineering A 923 (2025) 147704

Contents lists available at ScienceDirect

Materials Science & Engineering A

journal homepage: www.elsevier.com/locate/msea

Atomic resolution analysis of precipitates formed in an HPTE deformed Al-Mg-Si alloy

Vahid Tavakkoli [a,b], Lucas Brauch [b,c], Evgeniy Boltynjuk [a], Torsten Scherer [a,d], Andrey Mazilkin [a], Michael Eusterholz [d,e], Torben Boll [e], Yulia Ivanisenko [a,*], Christian Kubel [a,b,d,**]

[a] Institute of Nanotechnology, Karlsruhe Institute of Technology, Hermann-von-Helmholtz-Platz 1, Eggenstein-Leopoldshafen, 76344, Germany
[b] Department of Materials and Earth Sciences, Technical University of Darmstadt (TUD), 64287, Darmstadt, Germany
[c] Institute for Quantum Materials and Technologies, Karlsruhe Institute of Technology, Hermann-von-Helmholtz-Platz 1, Eggenstein-Leopoldshafen, 76344, Germany
[d] Karlsruhe Nano Micro Facility (KNMFi), Karlsruhe Institute of Technology, Hermann-von-Helmholtz-Platz 1, Eggenstein-Leopoldshafen, 76344, Germany
[e] Institute of Applied Materials (IAM-WK), Karlsruhe Institute of Technology, Hermann-von-Helmholtz-Platz 1, Eggenstein-Leopoldshafen, 76344, Germany

ARTICLE INFO

Keywords:
Severe plastic deformation
Al-Mg-Si alloy
Artificial aging
Precipitates

ABSTRACT

Improving both mechanical and electrical properties is one of the key requirements for reducing energy losses in power lines. Here, we investigate the structural evolution and hardening of Al 6101 grade, which is a versatile alloy known for its high electrical conductivity. Structure and properties changes were induced by severe plastic deformation followed by artificial aging. Nano indentation maps show improvement in hardness, which is connected to the formation of intermetallic phases. A range of hardening phases with different shapes and Mg/Si ratios have been identified by APT. HR(S)TEM imaging shows that the structure of most particles is only partially ordered due to the high defect density in severely deformed Al matrix. The observed particles exhibit several different crystalline structures, and their orientation relationships with the Al matrix differ from the ones previously established. Moreover, many nanometer sized precipitates consist of several different phases. These structural features are a consequence of non-equilibrium growth conditions of the precipitates and affect further thermal evolution as observed by DSC.

1. Introduction

Al-Mg-Si alloys are widely used in power generation and transfer, electronics, automotive, and aerospace industry due to their high electrical conductivity and strength, which can be attributed to secondary phase precipitates [1]. These alloys undergo solid solution treatment followed by artificial aging (AA) to enhance their properties. In the Al-Mg-Si system, precipitation of secondary phases during aging follows an established sequence, with the β″ and β′ phase playing a key role for strengthening. Attention has been paid to studying their crystal structure due to their significant impact on mechanical properties [2,3].

Andersen et al. reported the crystal structure of β″ based on modeling derived from exit wave reconstructed HRTEM images [4]. They determined the β″ unit cell to be monoclinic with space group *C2/m* and unit cell parameters a = 1.516 nm, b = 0.405 nm, c = 0.674 nm, β = 105.3° and a composition corresponding to Mg_6Si_5. However, Ninive et al. proposed a different β″ crystal structure. They reported that $Mg_4Al_3Si_4$ is the most likely composition of the precipitate with possible variations in a single particle. The β′ phase, $Mg_6Si_{3.3}$, has a rod-shape morphology, which precipitates along the <100> Al directions, and is coherent with the aluminum matrix along its c-axis. The structure is hexagonal with unit cell parameters a = 0.705 nm and c = 0.405 nm [5]. On the other hand, Vissers et al. showed in *ab-initio* calculations that the energetically most favorable unit cell for the β′ phase is expanded by a factor of 3 along the c-axis [6]. The intermediate phases U1, U2 and B′ are variants of the β′ phase. Their basic crystallographic information is summarized in Table S1 [6–15]. These precipitates have different effects on the mechanical and electrical properties due to a wide range of lattice misfits between the precipitates and the matrix. Zheng et al. investigated the microstructure evolution and precipitation behavior of an Al-Mg-Si

* Corresponding author. Institute of Nanotechnology, Karlsruhe Institute of Technology, Hermann-von-Helmholtz-Platz 1, Eggenstein-Leopoldshafen, 76344, Germany.
** Corresponding author. Institute of Nanotechnology, Karlsruhe Institute of Technology, Hermann-von-Helmholtz-Platz 1, Eggenstein-Leopoldshafen, 76344, Germany

https://doi.org/10.1016/j.msea.2024.147704
Received 3 July 2024; Received in revised form 21 October 2024; Accepted 19 December 2024
Available online 19 December 2024

alloy during aging. Their findings revealed that after aging at 170 °C for 6 h, the hardness reached a peak value of 127 HV, while the electrical conductivity remained relatively stable. This behavior was attributed to the formation of coherent precipitates, such as Mg/Si clusters and GP zones, alongside a reduction in solute atom concentration within the Al matrix [16].

The majority of structural studies have focused on fully annealed samples, where precipitate structures are well-defined. However, under non-equilibrium conditions after severe deformation, rapid precipitate growth occurs due to a high defect density, potentially altering the phases, their sequence and composition. Therefore, comprehensive studies on precipitates formed in non-equilibrium states, particularly through severe plastic deformation (SPD) followed by AA, are necessary to better understand processing conditions and their effect on properties of the industrially important Al-Mg-Si alloys. Valiev et al. [17] used high-pressure torsion (HPT) as a way to produce ultrafine-grained (UFG) structure in aluminum alloy 6101, which resulted in improved electrical conductivity and enhanced strength due to the presence of small precipitates. Sauvage et al. [18] conducted a comprehensive study on HPT-processed 6101 and 6102 aluminum alloys using transmission electron microscopy (TEM) and atom probe tomography (APT). Their findings indicated that the formation of an UFG structure with intra-granular nanoscale precipitates is an effective strategy to optimize the strength *vs.* conductivity trade-off in aluminum alloys. However, a detailed analysis of the structure of precipitates formed in SPD-processed Al alloys has not been conducted so far. Therefore, further studies are needed to understand the phase formation process under these non-equilibrium conditions.

The small volume fraction of secondary phases in the precipitation-hardened alloys renders conventional X-ray diffraction methods ineffective to establish the phase composition. TEM with selected area electron diffraction (SAED) [19], high-resolution imaging techniques like HR(S)TEM [20], and elemental analysis methods such as EDX and EELS are preferred for identifying nanoscale phases [21,22]. APT provides even more accurate information on secondary phase composition [23].

In our previous work [24], we revealed that the particles, which precipitate during AA, are responsible for the remarkable mechanical and electrical properties of the alloy. Here, we will demonstrate the change in microhardness of the alloy after AA and investigate the nature and evolution of the secondary phase particles formed under non-equilibrium conditions using APT and advanced analytical (S)TEM methods.

1.1. Material and methods

A 6101 grade Al alloy rods with chemical composition (at. %) 0.94 Mg, 1 Si, Fe $\leq$ 0.5, Cu $\leq$ 0.10, Zn $\leq$ 0.1, Cr $\leq$ 0.03, Mn $\leq$ 0.03 and Al balance was melted from high purity components. The initial samples were prepared in the shape of rolled rod with diameter of 11.8 mm and length of 34 mm. Samples were heated up to 500 °C for 1 h for solid solution treatment and quenched in water. The material had been deformed by high pressure torsion extrusion (HPTE) with a translational velocity of 3 mm/min and a rotation speed of 1 rpm (denoted as v3w1) at 100 °C. The applied HPTE process has been introduced in detail in Ref. [25]. AA was performed at 160 °C for 10 h.

The samples for TEM analysis were prepared using conventional electro-polishing. The samples were examined using a double aberration-corrected Themis Z transmission electron microscope (Thermo Fisher Scientific) operated at 300 kV and a probe corrected Themis 300 (Thermo Fisher Scientific) operated at 200 kV to reduce knock-on damage [26]. The software package JEMS has been used to index the FFTs of high-resolution images [27]. HAADF-STEM multi-slice image simulation was done using the software Prismatic 2.0 [28]. Elemental analysis was performed by means of energy dispersive X-ray spectroscopy (EDX) using a Super-X detector and analyzed by Velox 3.9.0. APT samples were prepared using the conventional lift-out method on a Strata 400 dual beam facility [29]. The APT analysis was performed on a LEAP 4000X HR instrument at 40 K with laser pulse energy of 30 pJ, and a pulse rate of 125 kHz. The APT reconstruction and data evaluation was performed with the APT Suite software 6.3 (CAMECA/AMETEK). The distribution of solutes was investigated using nearest neighbor (d-pair) distributions [30]. More details on the experimental procedure, in particularly on nano indentation and DSC can be found in the SI.

2. Results and discussion

Fig. 1a, b shows hardness maps for both the as-deformed sample and after AA. The maps show an increase in hardness as a result of the heat treatment. The average hardness of the sample after aging is 1.33 $\pm$ 0.07 GPa, while the as-deformed sample shows an average hardness of 1.14 $\pm$ 0.06 GPa (Fig. 1c). Our recent study shows that the main contribution to the increased mechanical properties is due to precipitation of secondary phases, which further leads to simultaneous improvement of the electrical properties [24].

The evolution of precipitates in the alloy after quenching, after HPTE and after AA at 160 °C was studied by means of APT. The presence of clusters or precipitates in the as-quenched state is difficult to detect, but they obviously develop during deformation and aging. The fifth nearest neighbor distribution for Mg is shown in Fig. S7 for the as-quenched and in Fig. 2a for the as-deformed states. For the condition after quenching, the average d-pair distance is slightly reduced compared to a randomized distribution, indicating a tendency of Mg atoms to correlate. In contrast, the pronounced shoulder in the Mg distribution in the as-deformed sample clearly indicates clustering. The corresponding Pearson correlation coefficient increases from 0.18 to 0.30. This result indicates the dynamical aging already occurring during the deformation [31,32].

These clusters can be assigned to GP zones, which are fully coherent with the matrix according to HRTEM images (Fig. S6). The clusters exhibit a diverse range of compositions, as indicated by the Mg/Si ratio distribution plot (Fig. 2), with a slight dominance of Mg-rich clusters, but also some Si-rich clusters present. This variable composition of GP zones has also been reported in previous studies [33]. However, while Fallah et al. claim that regardless of the alloy composition and aging history, the initial precipitates manifest as finely-dispersed Si-rich clusters, which subsequently undergo simultaneous coarsening and Mg-enrichment over time [34]. Our work indicates that in a highly defective structure produced by SPD, Mg-rich clusters also form at an early stage of precipitation.

The presence of the clusters and the high defect density introduced during HPTE changes the thermal evolution of the alloy as revealed by DSC analysis (Fig. 2c). For the quenched sample, several exothermic peaks are visible, which correspond to the known sequence of phase formation in this alloy [35]. The peak at low temperature is characteristic for the GP zone formation and the other peaks at higher temperatures correspond to a precipitation of secondary phases. For the deformed sample, only one broad peak is observed, and the corresponding heat release is noticeably smaller compared to that in the quenched counterpart. The absence of a peak for the GP zone formation can be explained by the fact that they had already formed during HPTE deformation (see APT and HRTEM results above). The peak onset temperature for HPTE sample is shifted to the left. This phenomenon is usually explained by a larger fraction of lattice defects, in particular grain boundaries, that not only dramatically enhance the diffusivity of alloying elements, but also increase the number of nucleation sites by decreasing the activation energy for precipitation formation [36,37].

For further characterization of the cluster evolution, an APT reconstruction of the aged sample has been performed. The reconstructed volume depicted in Fig. 2b reveals two discernible types of precipitates. One type are rod-shaped precipitates with an average length of ~15.2 $\pm$

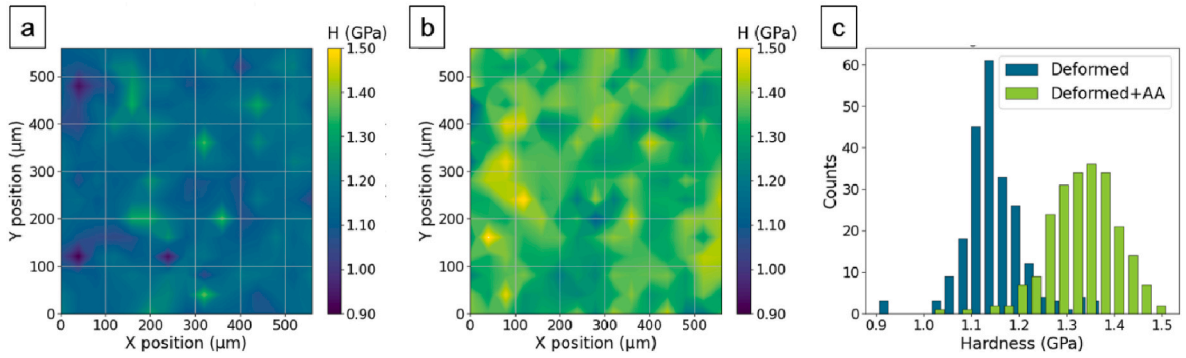

Fig. 1. Nanoindentation maps of deformed (a) and deformed + AA (b) samples. (c) Histograms of hardness for deformed and deformed + AA samples.

1 nm and diameter of ~3.1 ± 0.3 nm grown in $<002>_{Al}$ directions in agreement with reference [24], while the other type exhibit an irregular shape. This result is in line with the DF images shown in Fig. 3a. The Mg/Si composition distribution plots (right panels in Fig. 2a and b) exhibit one broad peak indicating the presence of a variety of phases. However, this Mg/Si composition range is narrower in AA160 sample than that in the deformed sample indicating a reduced variety of the composition. The average Mg/Si ratio is approximately 1.5, suggesting a potential association with β´ and/or β phases. The magnified views in both (a) and (b) reveal co-segregation and co-precipitation in two adjacent clusters (highlighted with a red circle), indicating that they nucleated in close proximity and subsequently grew until mutual contact. It is worth noting that Mg and Si clusters are present in both states, although their volume fraction is marginal. The presence of Mg clusters has already been observed by Murayama et al. [38] and the formation of Si clusters during quenching has been proposed for the Al-Si system by Edwards et al. [39]. However, it can be assumed that the Si clusters formed either as the result of the deformation process or excess of Si concentration in the matrix [40].

The DF-TEM image of the sample after AA at 160 °C in Fig. 3a reveals precipitates consistent in size and shape with the APT findings. According to our recently published study, the average diameter of the precipitates is 2.2 ± 0.9 nm, with a remarkably high precipitates number density (2.2 ± 0.5) × 10^{23} [24]. Fig. 3b displays the corresponding SAED, containing intense reflections of Al and weaker ones of the secondary phases. Table 1 lists interplanar distances measured from SAED to identify the phases. Multiple candidate phases match each d-value, complicating reliable phase composition determination, but in agreement with the Mg/Si APT analysis showing coexistence of several phases.

Therefore, HR(S)TEM imaging was used to identify the structure of individual precipitates. We found that most of the precipitates (~90 %) have a defective, polycrystalline structure, as shown in Fig. 4a. Most likely, defective structure of precipitates results from the accumulated strain induced by strong deformation during HPTE [41]. The corresponding FFT contains many reflections due to various structural motives and defects present in a single precipitate particle. Therefore, our efforts have been aimed at identifying the crystallography of individual particles with less distorted structure. Figs. 4 and 5 show a series of HR (S)TEM images of intermetallic particles present in the deformed and aged sample.

Fig. 4b shows a HRTEM micrograph of a particle with a core-shell structure. The corresponding FFT exhibits a spot pattern with six-fold symmetry and d-values of ~0.61 nm, which can be indexed as β´ phase with orientation relationship (OR): $[001]_{Al} \| [001]_{\beta'}$ and $[110]_{Al} \| [100]_{\beta'}$. The Fourier filtered image in Fig. S3 reveals the presence of an intermediate layer (~1 nm thickness). This feature has been reported before and suggested that an intermediate layer reduces the misfit strain between the β′ phase and the Al matrix. Furthermore, it has been suggested that this layer may facilitate coarsening, which would influence the mechanical properties [43–45]. Unlike in the bulk β′ structure, local compositional variations may be expected in the intermediate layer to optimize the local misfit [44]. However this goes beyond the structural and composition analysis performed here.

Another particle is shown in Fig. 4c. This particle demonstrates a $[001]_{Al} \| [010]_{\beta'}$ and $[210]_{Al} \| [1\bar{1}0]_{\beta'}$ OR. In addition, a number of reflections that do not belong to the Al or β´ phase are also observed in the FFTs in Fig. 4c, indicating that the precipitates are not single crystalline. The Fourier filtered images of the poly crystalline structure are shown in Fig. S2b. A coexistence of several phases in one particle has also been reported in a previous study [46].

A HRTEM image of another precipitate containing two crystallites with different structures is shown in Fig. 4d. The FFT of the upper part of the precipitate is in agreement with the U1 phase, whereas several phases/orientations are present in the lower precipitate.

Fig. 5 shows HRSTEM images of two β´ precipitates fitting the structure in Ref. [14]. Fig. 5a illustrates the six-fold symmetry of the atomic arrangement of Si in both of the two sublattice sites as shown in the magnified view in Fig. 5b. In this variant of the β´ phase, there are two Si positions. The projected atomic structure is in agreement with the higher intensity for the Si atoms in the 4e Wyckoff position compared to the Si in the 2d Wyckoff position. The position of the Mg atomic columns is almost invisible in the HAADF-STEM image in agreement with the image simulation (Fig. 5c).

A HRSTEM image of another β´ particle acquired by STEM-iDPC is shown in Fig. 5d with the Al lattice superimposed on the precipitate structure. To separate the matrix and the particle, we performed Fourier filtering using the reflections from Al (Fig. S2a) and from the β´phase (Fig. S2b). The combination of these two filtered images is shown in Fig. 5f, where columns of Si atoms in two different positions in the β´ lattice are clearly visible as it is also shown in the magnified view in Fig. 5b. The integrated EDX spectrum of this phase shows a Mg/Si ratio of 1.8, which is characteristic for the β´ phase (Fig. S3).

The precipitate in Fig. 5a shows a $[001]_{Al} \| [001]_{\beta'}$ and $[3\bar{4}0]_{Al} \| [100]_{\beta'}$ OR, whereas the precipitate in Fig. 5d reveals a $[001]_{Al} \| [001]_{\beta'}$ and $[100]_{Al} \| [100]_{\beta'}$ OR with a semi-coherent phase boundary with the matrix since the $(003)_{\beta'}$ reflection coinciding with the $(200)_{Al}$ reflection (see inset in Fig. 5c).

The precipitates examined by HR(S)TEM exhibit a (semi)coherent structure. It should be noted that detailed HR(S)TEM analysis was carried out only for particles with well resolvable crystal structure; for many precipitates this was not possible. This is because most of precipitates exhibit a high defect density, consist of more than one grain, or their orientation does not allow obtaining images with atomic resolution. In this case, as mentioned above, the number density of precipitates is extremely high. This is obviously due to the increased number of nucleation centers created during SPD and determines high mechanical properties of the material. i.e., its enhanced strain hardening capacity and ductile behavior [24]. Recently, several studies have been published

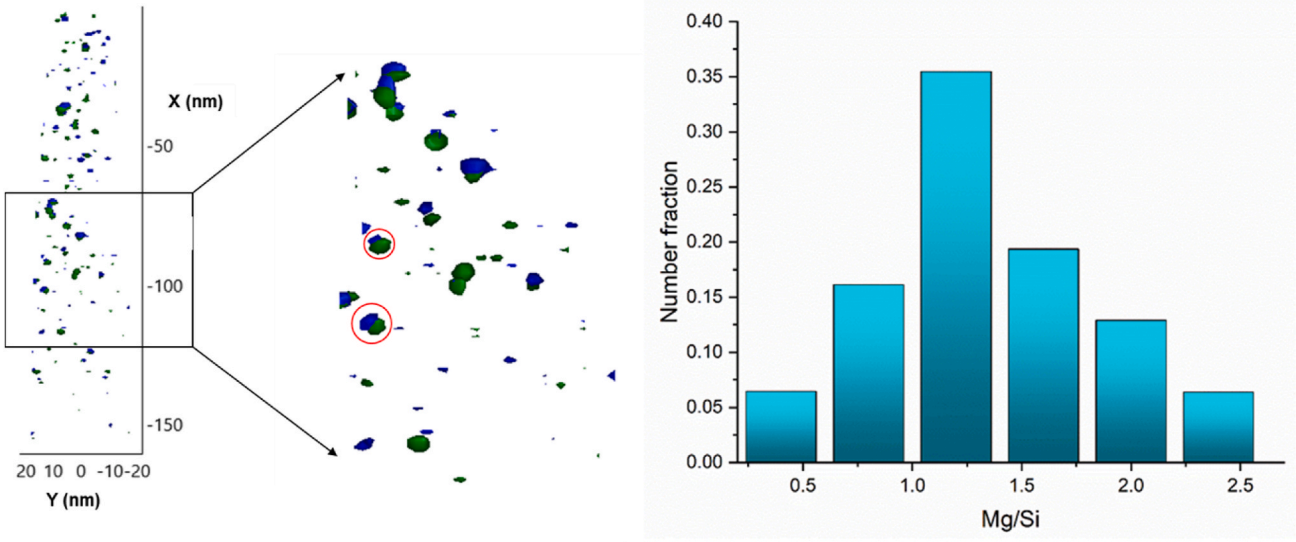

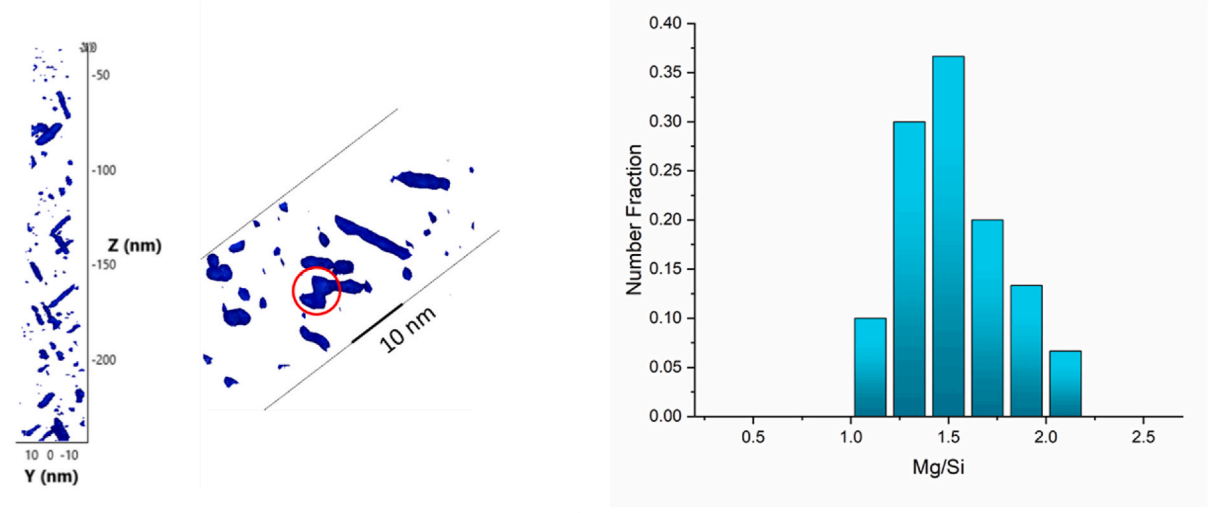

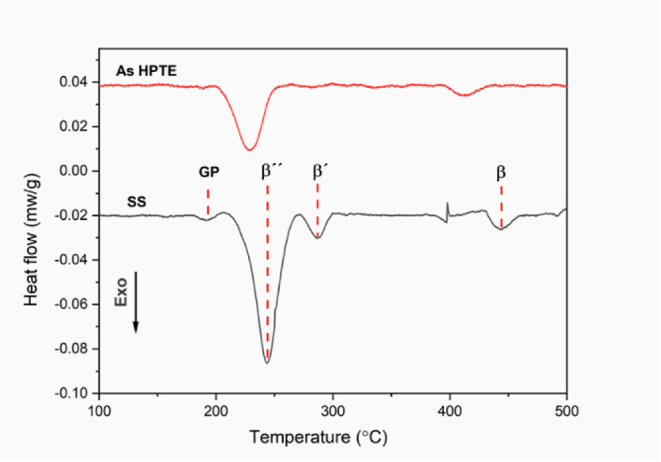

Fig. 2. 3D reconstructed volume of clusters visualized using iso-compositional surfaces of 4.0 at. % Mg (blue) and 3.0 at.% Si (green) indicating precipitates (a) in the as-deformed state and (b) after AA 160 °C with a magnified view of the coprecipitation of two neighboring clusters marked by red circles. Corresponding histograms show the distribution of the Mg/Si ratio in the precipitates. (c) DSC curves of as-quenched sample after solid solution treatment (SS) and as-HPTE sample. (For interpretation of the references to colour in this figure legend, the reader is referred to the Web version of this article.)

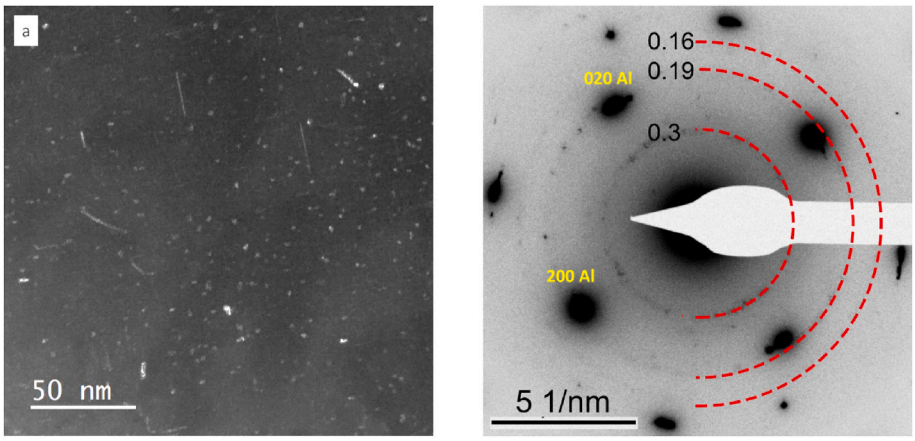

Fig. 3. (a) DF image of the deformed sample after AA at 160 °C; (b) DP with the overlaid semi-circles for the measured d-values of the secondary phases and two reflections from the Al grain.

Table 1
d-values measured from the DP compared with possible candidate phases in Table S1.

$d_{measured}$ [nm]	β″ [4]		β′ [14]		U1 [42]		U2 [11]	
	hkl	d [nm]	hkl	d [nm]	hkl	d [nm]	hkl	d [nm]
0.30	$31\bar{1}$	0.30	201	0.30	011	0.31	201	0.31
0.19	$22\bar{1}$	0.19	201	0.19	103	0.19	311	0.19
0.16	$71\bar{3}$	0.16	223	0.16			222	0.16

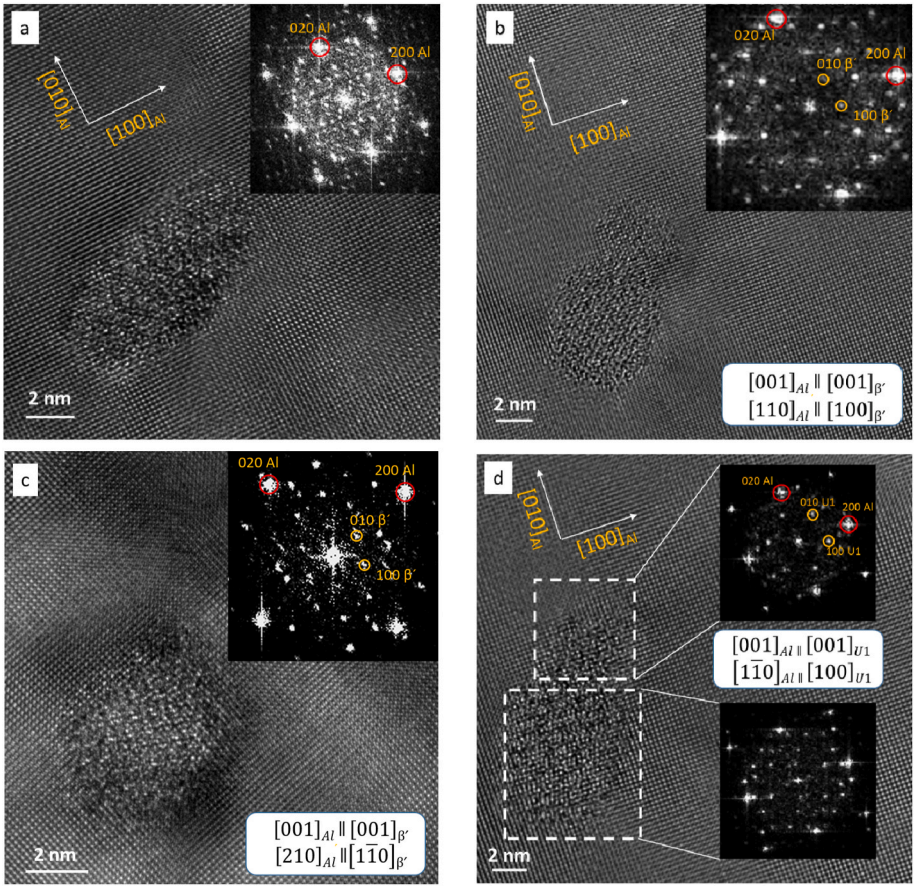

Fig. 4. HRTEM micrograph and corresponding FFT of (a) distorted phase. (b, c) β′phase particles with two different ORs, and (d) a precipitate of partially U1 and of non-indexed structure. The insets show the ORs between particle and matrix. The simulated diffraction patterns are shown in Fig. S1.

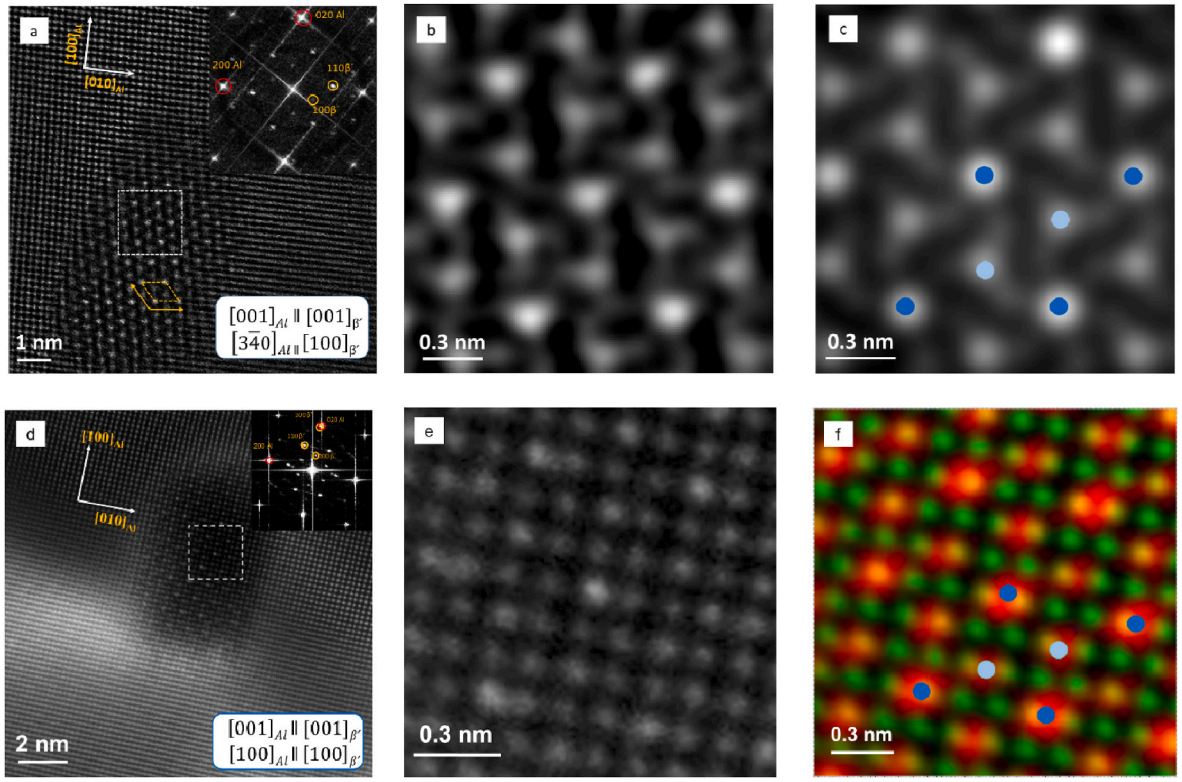

Fig. 5. (a, d) HRSTEM images of β´ phase with corresponding FFT (inset); yellow diamond shape in (a) shows the β´ unit cell along the c-axis; (b, e) magnified views of white dashed square areas in (a, d); (c) simulated HAAFD-STEM image of β´ phase; (f) inversed FFT image of β´ phase in (d). Dark and light blue circles show the position of Si1 and Si2. (For interpretation of the references to colour in this figure legend, the reader is referred to the Web version of this article.)

establishing the ORs and their role in determining precipitate morphology for various precipitates in Al-Mg-Si alloys [45,47,48]. These studies report that the morphology of precipitates in the equilibrium state is determined by anisotropic misfit strain, which depends on the mutual orientation of the phase and matrix lattices. In our study, we discovered several ORs that have not been previously reported, whose presence seems to be associated with the growth of precipitates in a highly defective state. Since the thermal activation during AA was low, the primary driving force for phase transformation is the energy accumulated during deformation, which is associated with the high defect density. The high solute diffusivity in a defective structure can lead to fast atomic transport to form a precipitate with growth directions determined by the local diffusion flux conditions. Another feature observed in the alloy after AA, which is presumably associated with the high defect density, is the coprecipitation of particles (see Figs. 2 and 4d), when dislocations and grain boundaries provide many nucleation sites in close proximity.

Considering these structural features helps to understand the DSC measurements of the HPTE deformed sample (Fig. 2) with only one broad exothermal peak at a temperature slightly below the typical β″ precipitation temperature and with a significantly reduced heat release compared to that in the as quenched reference. A large number of GP zones have already formed during HPTE and apparently no significant additional GP zone formation occurs during further heating. Based on our HR(S)TEM studies the broad DSC peak in deformed sample has to be interpreted as a convolution of heat releases of several phases, which precipitate simultaneously in this temperature range, presumably due to the high solute mobility induced by the high defect density. The reduced heat release in the deformed state is presumably related to a reduced volume fraction of precipitated particles in the deformed sample and the high defect density in the particles and their unusual and presumably energetically less favorable ORs, leading to a smaller amount of energy being released during their precipitation.

Finally, we can hypothesize that control of OR, particle morphology, and their number density through changes in material processing parameters allows to tailor the microstructure of Al alloys to achieve optimal properties for specific applications.

3. Conclusions

A combination of nanohardness measurements, HR(S)TEM imaging with EDX and APT analysis was employed to explore the mechanical properties and structural evolution of precipitates in a HPTE deformed Al 6101 alloy followed by AA at 160 °C. The APT study shows that although some clustering is already present in the as-quenched state, a noticeable evolution of the phase composition with the formation of clusters having different Mg/Si ratios starts during HPTE deformation. The phase formation process is significantly influenced by the high defect density, as indicated by DSC measurements. The coexistence of several crystalline phases within the alloy results in an improved hardness. Their structure is closely related to the known structure of precipitates in Al-Mg-Si alloys, but noticeable variations have been observed due to deformation-induced defects. These secondary phase precipitates exhibit either partially defective and/or polycrystalline structures, partially as core-shell structures, because of the highly defective state of the Al matrix. Several OR variants have been detected, which are not typically observed in this alloy group with common processing conditions.

CRediT authorship contribution statement

Vahid Tavakkoli: Writing – original draft. **Lucas Brauch:** Methodology. **Evgeniy Boltynjuk:** Methodology. **Torsten Scherer:** Resources. **Andrey Mazilkin:** Supervision. **Michael Eusterholz:** Methodology. **Torben Boll:** Methodology. **Yulia Ivanisenko:** Supervision, Methodology. **Christian Kubel:** Supervision.

Disclosure statement

No potential conflict of interest was reported by the authors.

Data availability

The raw data required to reproduce these findings are available to download from https://doi.org/10.35097/1780.

Orginality statement

I write on behalf of myself and all co-authors to confirm that the results reported in the manuscript are original and neither the entire work, nor any of its parts have been previously published. The authors confirm that the article has not been submitted to peer review, nor has been accepted for publishing in another journal. The author(s) confirms that the research in their work is original, and that all the data given in the article are real and authentic. If necessary, the article can be recalled, and errors corrected.

Funding

This work was supported by German Academy Exchange Service (DAAD).

Declaration of competing interest

The authors declare that they have no known competing financial interests or personal relationships that could have appeared to influence the work reported in this paper.

Acknowledgments

The authors gratefully acknowledge Karlsruhe Nano Micro Facility (KNMFi) for providing advanced instruments (proposal number: ha031456). This research has been performed as part of the Helmholtz Joint Laboratory Model Driven Materials Characterization (MDMC). We are thankful to Maxim Murashkin for fruitful discussions, Delphine Chassaing for APT analysis and Jing Lin for DSC measurements.

Appendix A. Supplementary data

Supplementary data to this article can be found online at https://doi.org/10.1016/j.msea.2024.147704.

Data availability

Data will be made available on request.

References

[1] I. Polmear, D. StJohn, J.-F. Nie, M. Qian, Light Alloys: Metallurgy of the Light Metals, Butterworth-Heinemann, 2017.
[2] K. Ma, et al., Coupling of dislocations and precipitates: impact on the mechanical behavior of ultrafine grained Al–Zn–Mg alloys, Acta Mater. 103 (2016) 153–164, https://doi.org/10.1016/j.actamat.2015.09.017.
[3] S.N. Khangholi, M. Javidani, A. Maltais, X.-G. Chen, Effects of natural aging and pre-aging on the strength and electrical conductivity in Al-Mg-Si AA6201 conductor alloys, Mater. Sci. Eng., A 820 (2021) 141538, https://doi.org/10.1016/j.msea.2021.141538.
[4] S.J. Andersen, H.W. Zandbergen, J. Jansen, C. TrÆholt, U. Tundal, O. Reiso, The crystal structure of the β″ phase in Al–Mg–Si alloys, Acta Mater. 46 (9) (1998) 3283–3298, https://doi.org/10.1016/S1359-6454(97)00493-X.
[5] P.H. Ninive, et al., Detailed atomistic insight into the β″ phase in Al–Mg–Si alloys, Acta Mater. 69 (2014) 126–134, https://doi.org/10.1016/j.actamat.2014.01.052.
[6] R. Vissers, M.A. v van Huis, J. Jansen, H.W. Zandbergen, C.D. Marioara, S. J. Andersen, The crystal structure of the β′ phase in Al–Mg–Si alloys, Acta Mater. 55 (11) (2007) 3815–3823.
[7] C.D. Marioara, S.J. Andersen, J. Jansen, H.W. Zandbergen, Atomic model for GP-zones in a 6082 Al-Mg-Si system, Acta Mater. 49 (2) (2001) 321–328, https://doi.org/10.1016/S1359-6454(00)00302-5.
[8] K. Matsuda, et al., High-resolution electron microscopy on the structure of Guinier-Preston zones in an Al-1.6 mass Pct Mg2Si alloy, Metall. Mater. Trans. A 29 (4) (1998) 1161–1167, https://doi.org/10.1007/s11661-998-0242-7.
[9] S.J. Andersen, et al., Directionality and column arrangement principles of precipitates in Al-Mg-Si-(Cu) and Al-Mg-Cu linked to line defect in Al, Mater. Sci. Forum 877 (2017) 461–470.
[10] S.J. Andersen, C.D. Marioara, R. Vissers, A. Frøseth, H.W. Zandbergen, The structural relation between precipitates in Al–Mg–Si alloys, the Al-matrix and diamond silicon, with emphasis on the trigonal phase U1-MgAl2Si2, Mater. Sci. Eng., A 444 (1–2) (2007) 157–169.
[11] S.J. Andersen, C.D. Marioara, A. Frøseth, R. Vissers, H.W. Zandbergen, Crystal structure of the orthorhombic U2-Al4Mg4Si4 precipitate in the Al–Mg–Si alloy system and its relation to the β′ and β″ phases, Mater. Sci. Eng., A 390 (1) (2005) 127–138, https://doi.org/10.1016/j.msea.2004.09.019.
[12] K. Matsuda, et al., Precipitation sequence of various kinds of metastable phases in Al-1.0mass% Mg2Si-0.4mass% Si alloy, J. Mater. Sci. 35 (1) (2000) 179–189, https://doi.org/10.1023/A:1004769305736.
[13] S.D. Dumolt, D.E. Laughlin, J.C. Williams, Formation of a modified β′ phase in aluminum alloy 6061, Scripta Metall. 18 (12) (1984) 1347–1350, https://doi.org/10.1016/0036-9748(84)90362-4.
[14] R. Vissers, M.A. van Huis, J. Jansen, H.W. Zandbergen, C.D. Marioara, S. J. Andersen, The crystal structure of the β′ phase in Al-Mg-Si alloys, Acta Mater. 55 (11) (2007) 3815–3823, https://doi.org/10.1016/j.actamat.2007.02.032.
[15] N.A. Bul'enkov, A.G. Yakovenko, O.M. Ul'yanikhina, X-ray diffraction study of the Mg2Si-Mg2Ge system, J. Struct. Chem. 11 (6) (1971) 1059–1061.
[16] Y. Zheng, B. Luo, W. Xie, W. Li, Microstructure evolution and precipitation behavior of Al-Mg-Si alloy during initial aging, China Foundry 20 (1) (2023) 57–62.
[17] R.Z. Valiev, M.Y. Murashkin, I. Sabirov, A nanostructural design to produce high-strength Al alloys with enhanced electrical conductivity, Scripta Mater. 76 (2014) 13–16, https://doi.org/10.1016/j.scriptamat.2013.12.002.
[18] X. Sauvage, E.V. Bobruk, M.Y. Murashkin, Y. Nasedkina, N.A. Enikeev, R.Z. Valiev, Optimization of electrical conductivity and strength combination by structure design at the nanoscale in Al-Mg-Si alloys, Acta Mater. 98 (2015) 355–366, https://doi.org/10.1016/j.actamat.2015.07.039.
[19] D.B. Williams, C.B. Carter, D.B. Williams, C.B. Carter, The Transmission Electron Microscope, Springer, 1996.
[20] T.-F. Chung, et al., HR-STEM investigation of atomic lattice defects in different types of η precipitates in creep-age forming Al–Zn–Mg–Cu aluminium alloy, Mater. Sci. Eng., A 815 (2021) 141213, https://doi.org/10.1016/j.msea.2021.141213.
[21] H. Chen, et al., Atomic scale investigation of the crystal structure and interfaces of the B′ precipitate in Al-Mg-Si alloys, Acta Mater. 185 (2020) 193–203, https://doi.org/10.1016/j.actamat.2019.11.059.
[22] E.A. Mørtsell, S. Wenner, P. Longo, S.J. Andersen, C.D. Marioara, R. Holmestad, Elemental electron energy loss mapping of a precipitate in a multi-component aluminium alloy, Micron 86 (2016) 22–29.
[23] M.W. Zandbergen, A. Cerezo, G.D.W. Smith, Study of precipitation in Al–Mg–Si Alloys by atom probe tomography II. Influence of Cu additions, Acta Mater. 101 (2015) 149–158, https://doi.org/10.1016/j.actamat.2015.08.018.
[24] V. Tavakkoli, et al., Precipitate-mediated enhancement of mechanical and electrical properties in HPTE-processed Al–Mg–Si alloy, Mater. Sci. Eng., A (2024) 146556, https://doi.org/10.1016/j.msea.2024.146556.
[25] Y. Ivanisenko, et al., High Pressure Torsion Extrusion as a new severe plastic deformation process, Mater. Sci. Eng., A 664 (2016) 247–256, https://doi.org/10.1016/j.msea.2016.04.008.
[26] E. Thronsen, et al., The effect of heavy deformation on the precipitation in an Al-1.3Cu-1.0Mg-0.4Si wt.% alloy, Mater. Des. 186 (2020) 108203, https://doi.org/10.1016/j.matdes.2019.108203.
[27] P. Stadelmann, Image analysis and simulation software in transmission electron microscopy, Microsc. Microanal. 9 (S03) (2003) 60–61.
[28] L. Rangel DaCosta, et al., Prismatic 2.0 – simulation software for scanning and high resolution transmission electron microscopy (STEM and HRTEM), Micron 151 (2021) 103141, https://doi.org/10.1016/j.micron.2021.103141.
[29] D.J. Larson, et al., History of APT and LEAP," *Local Electrode Atom Probe Tomogr*, A User's Guid, 2013, pp. 1–23.
[30] L.T. Stephenson, M.P. Moody, P. V Liddicoat, S.P. Ringer, New techniques for the analysis of fine-scaled clustering phenomena within atom probe tomography (APT) data, Microsc. Microanal. 13 (6) (2007) 448–463.
[31] M. Cai, D.P. Field, G.W. Lorimer, A systematic comparison of static and dynamic ageing of two Al–Mg–Si alloys, Mater. Sci. Eng., A 373 (1–2) (2004) 65–71.
[32] H.J. Roven, M. Liu, J.C. Werenskiold, Dynamic precipitation during severe plastic deformation of an Al-Mg-Si aluminium alloy, Mater. Sci. Eng., A 483 (484) (2008) 54–58, https://doi.org/10.1016/j.msea.2006.09.142, 1-2 C.
[33] T. Saito, et al., Atomic structures of precipitates in Al–Mg–Si alloys with small additions of other elements, Adv. Eng. Mater. 20 (7) (2018) 1800125.
[34] V. Fallah, B. Langelier, N. Ofori-Opoku, B. Raeisinia, N. Provatas, S. Esmaeili, Cluster evolution mechanisms during aging in Al–Mg–Si alloys, Acta Mater. 103 (2016) 290–300, https://doi.org/10.1016/j.actamat.2015.09.027.
[35] I. Hamdi, Z. Boumerzoug, F. Chabane, Study of precipitation kinetics of an Al-Mg-Si alloy using differential scanning calorimetry, Acta Metall. Slovaca 23 (2) (2017) 155–160.

[36] S.K. Panigrahi, R. Jayaganthan, V. Pancholi, M. Gupta, A DSC study on the precipitation kinetics of cryorolled Al 6063 alloy, Mater. Chem. Phys. 122 (1) (2010) 188–193, https://doi.org/10.1016/j.matchemphys.2010.02.032.
[37] G. Angella, P. Bassani, A. Tuissi, D. Ripamonti, M. Vedani, Microstructure evolution and aging kinetics of Al-Mg-Si and Al-Mg-Si-Sc alloys processed by ECAP, Nanomaterials by Severe Plastic Deformation 503 (2006) 493–498. https://doi.org/10.4028/www.scientific.net/MSF.503-504.493.
[38] M. Murayama, K. Hono, M. Saga, M. Kikuchi, Atom probe studies on the early stages of precipitation in Al–Mg–Si alloys, Mater. Sci. Eng., A 250 (1) (1998) 127–132.
[39] G.A. Edwards, K. Stiller, G.L. Dunlop, M.J. Couper, THE PRECIPITATION SEQUENCE IN Al ± Mg ± Si ALLOYS 46 (11) (1998) 3893–3904.
[40] L. Zhen, W.D. Fei, S.B. Kang, H.W. Kim, Precipitation behaviour of Al-Mg-Si alloys with high silicon content, J. Mater. Sci. 32 (7) (1997) 1895–1902, https://doi.org/10.1023/A:1018569226499.
[41] Y. Weng, et al., Effect of pre-straining on structure and formation mechanism of precipitates in Al–Mg–Si–Cu alloy, Trans. Nonferrous Metals Soc. China 32 (2) (2022) 436–447.
[42] S.J. Andersen, C.D. Marioara, R. Vissers, A. Frøseth, H.W. Zandbergen, The structural relation between precipitates in Al-Mg-Si alloys, the Al-matrix and diamond silicon, with emphasis on the trigonal phase U1-MgAl2Si2, Mater. Sci. Eng., A 444 (1–2) (2007) 157–169, https://doi.org/10.1016/j.msea.2006.08.084.
[43] S. Gulbrandsen-Dahl, K.O. Pedersen, C. Marioara, M. Kolar, K. Marthinsen, Effect of precipitates/effect of microstructure: mechanical characteristics of post-β″ precipitates in Al–Mg–Si alloys. Proc. 11th Intern. Conf. Alum. Alloy, 2008, pp. 1634–1640. Available: https://www.scopus.com/inward/record.uri?eid=2-s2.0-84865234103&partnerID=40&md5=3adcf44ec1f3519da9aec75523d61dae.
[44] K. Teichmann, C.D. Marioara, S.J. Andersen, K. Marthinsen, TEM study of β′ precipitate interaction mechanisms with dislocations and β′ interfaces with the aluminium matrix in Al–Mg–Si alloys, Mater. Char. 75 (2013) 1–7, https://doi.org/10.1016/j.matchar.2012.10.003.
[45] Z.-J. Zhao, et al., Orientation relationship prediction and interfacial structure of a nano-scale Si-Mg2Si core–shell precipitate in an aluminum alloy, Mater. Lett. 350 (2023) 134967, https://doi.org/10.1016/j.matlet.2023.134967.
[46] T. Maeda, et al., Structural and compositional study of precipitates in under-aged Cu-added Al-Mg-Si alloy, Sci. Rep. 8 (1) (2018) 16629, https://doi.org/10.1038/s41598-018-35134-8.
[47] Y. Weng, Z. Jia, L. Ding, S. Muraishi, X. Wu, Q. Liu, The multiple orientation relationships and morphology of β' phase in Al-Mg-Si-Cu alloy, J. Alloys Compd. 767 (2018) 81–89, https://doi.org/10.1016/j.jallcom.2018.07.077.
[48] W. Yang, M. Wang, Y. Jia, R. Zhang, Studies of orientations of β″ precipitates in Al-Mg-Si-(Cu) alloys by electron diffraction and transition matrix analysis, Metall. Mater. Trans. A 42 (9) (2011) 2917–2929, https://doi.org/10.1007/s11661-011-0680-5.